frontiers | Frontiers in Physics

TYPE Review
PUBLISHED 01 November 2022
DOI 10.3389/fphy.2022.1028258

OPEN ACCESS

EDITED BY
Xueli Chen,
Xidian University, China

REVIEWED BY
Yihan Wang,
Xidian University, China
Sung-Liang Chen,
Shanghai Jiao Tong University, China

*CORRESPONDENCE
Xosé Luís Deán-Ben,
xl.deanben@pharma.uzh.ch

SPECIALTY SECTION
This article was submitted to Medical Physics and Imaging,
a section of the journal
Frontiers in Physics

RECEIVED 25 August 2022
ACCEPTED 04 October 2022
PUBLISHED 01 November 2022

CITATION
Deán-Ben XL and Razansky D (2022), A practical guide for model-based reconstruction in optoacoustic imaging.
Front. Phys. 10:1028258.
doi: 10.3389/fphy.2022.1028258

A practical guide for model-based reconstruction in optoacoustic imaging

Xosé Luís Deán-Ben[1,2]* and Daniel Razansky[1,2]

[1]Faculty of Medicine, Institute of Pharmacology and Toxicology and Institute for Biomedical Engineering, University of Zurich, Zurich, Switzerland, [2]Department of Information Technology and Electrical Engineering, Institute for Biomedical Engineering, ETH Zurich, Zurich, Switzerland

Optoacoustic (OA, photoacoustic) imaging capitalizes on the low scattering of ultrasound within biological tissues to provide optical absorption-based contrast with high resolution at depths not reachable with optical microscopy. For deep tissue imaging applications, OA image formation commonly relies on acoustic inversion of time-resolved tomographic data. The excitation of OA responses and subsequent propagation of ultrasound waves can be mathematically described as a forward model enabling image reconstruction *via* algebraic inversion. These model-based reconstruction methods have been shown to outperform alternative inversion approaches and can further render OA images from incomplete datasets, strongly distorted signals or other suboptimally recorded data. Herein, we provide a general perspective on model-based OA reconstruction methods, review recent progress, and discuss the performance of the different algorithms under practical imaging scenarios.

KEYWORDS

optoacoustic imaging, photoacoustic imaging, model-based reconstruction, compressed-sensing, partial data acquisition, high-frame-rate imaging, super-resolution imaging

1 Introduction

Development, implementation and optimization of image formation algorithms is essential for advancing the performance of biomedical imaging modalities [1–3]. Optoacoustic (OA, photoacoustic) imaging has experienced an unprecedented growth in the last 10–15 years to become a powerful technology covering a large range of spatial and temporal imaging scales and providing otherwise-unavailable functional and molecular information deep from living tissues [4–8]. Rapid evolution of the OA technology has resulted in a myriad of embodiments based on different light delivery and ultrasound (US) detection methods [9–12]. Various types of sensors with detection bandwidth tailored to the desired resolution-depth range [13–16] and acquisition geometries (i.e. spatial distribution of US detectors relative to the sample) have further been developed [17–22]. Many of these systems have found use in biomedical research studies and clinical applications [23–28]. The great diversity of possible hardware designs represents an important advantage of the OA technology [29]. On the other hand, significant variability of image formation approaches, independently developed for each particular configuration [30–33], may compromise reproducibility and reliability of the reported experimental results thus hindering the development of standardized methodologies enabling accurate quantification of bio-markers [34].

OA is inherently a tomographic imaging modality. This implies that OA images can only be accurately reconstructed if signals are acquired at a set of locations enclosing the sample with sufficient angular coverage [35–37]. OA excitation is mainly performed with short (10^{-10}–10^{-7} s) light pulses. In this case, the collected signals around the sample correspond to a solution of an initial value problem expressed as a Radon-type transform that depends on the arrangement and shape of US sensors [38–40]. Much like for x-ray CT, analytical inversion can be performed by means of a filtered back-projection (FBP) formula, which in practice is discretized to reconstruct an image from a finite number of signals [41–44]. However, accurate image reconstruction implies a more complex representation of the physical problem. The negative impact of insufficient spatial sampling and noise in tomographic imaging with FBP algorithms has long been recognized [45]. Note that the OA forward model corresponds to a different type of transform than that in x-ray CT, but the term FBP is also used in the OA literature as it is conceptually equivalent. The shape and detection bandwidth of the sensors as well as acoustic propagation effects cannot accurately be accounted for by FBP formulas, which have only been developed for specific acquisition or scanning geometries. Model-based (MB) inversion schemes, which determine the desired solution (reconstructed image) *via* minimization of a cost function, are known to overcome the major limitations of FBP algorithms [39, 46–48]. Apart from the so-called data fidelity term, the cost function can additionally include regularization terms penalizing unlikely solutions given the available *a priori* knowledge on the sample [49–56]. Also, the solution can be constrained e.g. not to have negative values having no physical meaning [57–59]. Another important aspect to consider is the fact that the admissible solutions of the tomographic inversion problem can be restricted by expressing the images as a combination of a set of basis functions. Proper selection of these functions along with regularization terms enable exploiting compressed-sensing-based concepts to reconstruct an image from a relatively low number of signals [60–62]. Generally, MB reconstruction provides a flexible framework for the reconstruction of OA images and is generally applicable for any physical configuration.

In this review article, we provide a practical guide for MB reconstruction in OA imaging. We focus on describing the enhanced performance with respect to alternative reconstruction algorithms rather than on the mathematical foundations, which are briefly discussed without loss of generality for short-pulsed excitation. We further show that MB reconstruction enables capabilities unattainable with conventional reconstruction approaches, such as super-resolution imaging beyond the acoustic diffraction barrier, image reconstruction using a single detector or high-resolution imaging through the skull bone.

2 The optoacoustic forward model

In practice, MB reconstruction is performed by considering a discrete-to-discrete linear model mapping a finite-dimensional representation of the optical absorption distribution to the collected signals at a set of locations and time points. The mathematical derivation of the OA forward model depends on the temporal profile of the light beam and can be done in the time or frequency domains [63–65]. Without loss of generality, we briefly describe below the time-domain model for standard short-pulsed excitation verifying the so-called stress and thermal confinement conditions [66] (Figure 1A). In this case, the temporal profile of the light beam can be approximated as a Dirac delta $\delta(t)$ and optical absorption results in an initial pressure rise $p_0(\mathrm{r}) = \Gamma(r)H(r)$, being $\Gamma(r)$ the dimensionless Grueneisen parameter and $H(r)$ the energy being thermalized per unit volume. Propagation of an US wave optoacoustically generated in soft tissues is mathematically described by [67]

$$\frac{\partial^2 p(r,t)}{\partial t^2} - c(r)^2 \rho(r) \nabla \cdot \left(\frac{1}{\rho(r)} \nabla p(r,t) \right) = \Gamma(r) H(r) \frac{\partial \delta(t)}{\partial t}, \tag{1}$$

being $p(r,t)$ the acoustic pressure field, $c(r)$ the speed of sound and $\rho(r)$ the mass density of the medium. Equation 1 corresponds to a wave equation with a well-defined source term that can be expressed as an initial value problem [67], hence a mathematical solution exists. Generally, the pixels (or voxels) of a Cartesian grid enclosing the sample are considered to build the basis functions used to approximate $H(r)$ e.g. *via* weighted interpolation (Figure 1B) [68, 69], i.e., Eq. 1 is approximated by

$$\frac{\partial^2 p(r,t)}{\partial t^2} - c(r)^2 \rho(r) \nabla \cdot \left(\frac{1}{\rho(r)} \nabla p(r,t) \right) \approx \frac{\partial \delta(t)}{\partial t} \sum_{i=1}^{N} p_{0,i} k_i(r), \tag{2}$$

where $p_{0,i}$ is the initial pressure at the center of the ith voxel and $k_i(r)$ is the interpolation function. The solution of Eq. 2 can be expressed as

$$p(r,t) = \sum_{i=1}^{N} p_{0,i} p_i(r,t), \tag{3}$$

where $p_i(r,t)$ is the generated pressure field for a unit initial pressure rise at the ith voxel. An analytical expression of $p_i(r,t)$ can be derived in some cases, e.g. for a uniform non-attenuating acoustic medium [48]. Note that soft tissues are modelled as a heterogeneous fluid in Eq. 1. The wave equation can be significantly more complex for hard (solid) and/or absorbing tissues such as the skull bone [70]. However, an initial value

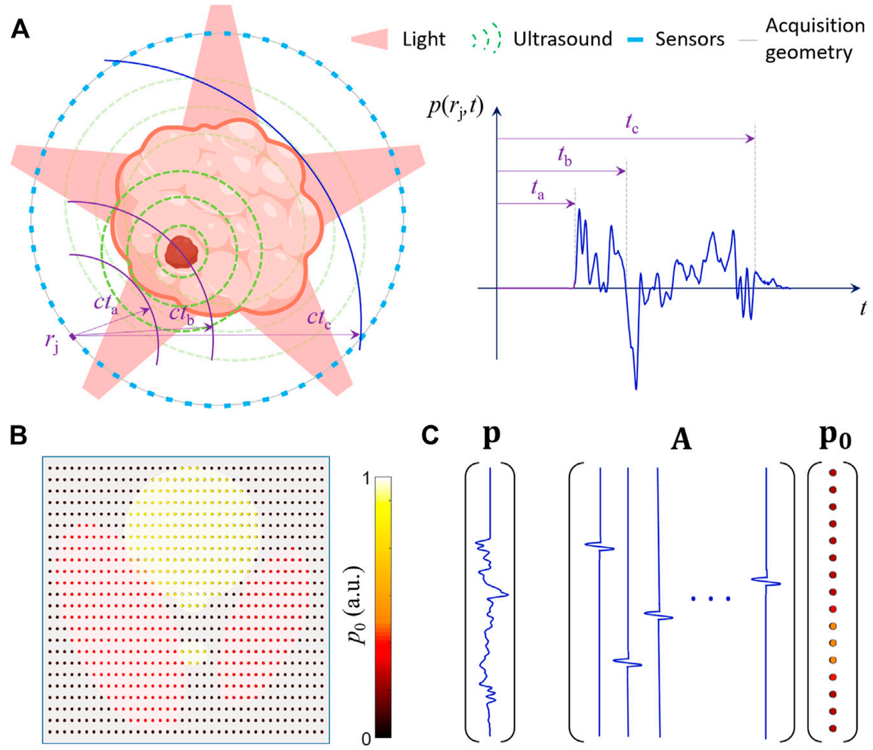

FIGURE 1
Time-domain optoacoustic (OA) forward model for short-pulsed excitation. **(A)** Schematic representation of the excitation of ultrasound (US) waves with light. An example of time-resolved OA signal is shown. For a uniform acoustic medium with a defined speed of sound, the time-of-flight linearly scales with the distance to the measuring location. **(B)** Discretization of the OA image by considering the initial pressure at a define grid of points. **(C)** Discrete-to-discrete OA forward model expressed in a matrix form mapping the initial pressure expressed as a column vector to the measured pressure at different time points also expressed as a column vector. The columns of the model-matrix correspond to the pressure signals for a unit initial pressure at the corresponding pixel (or voxel). Note that only one collected signal is shown and the model-matrix is generally built by considering multiple measuring locations.

problem can still be defined, thus the time-resolved $p_i(r,t)$ signals for all voxels can be obtained e.g. with numerical simulations [30]. Alternatively, these can be measured experimentally by scanning a sub-resolution absorber [71]. This approach further enables accounting for the response of the US transducer(s) used to collect the OA signals. In this case, $p_i(r,t)$ corresponds to the collected voltage signals rather than the pressure field, which are affected by the transducer response and can also be theoretically modelled [72–74]. The discrete-to-discrete OA forward model is built from the values of $p_i(r,t)$ for the positions of the transducer(s) and the sampling instants. Specifically, $p(r,t)$ at these positions and instants, expressed as a column vector $\mathbf{p}$, is given as a function of $p_{0,i}$ for the voxels of the grid, also expressed as a column vector $\mathbf{p_0}$, as

$$\mathbf{p} = \mathbf{A}\mathbf{p_0}. \tag{4}$$

The model matrix $\mathbf{A}$ represents the discrete-to-discrete OA forward model. The columns of this matrix correspond to the $p_i(r,t)$ signals for each voxel of the grid (Figure 1C). If the reconstruction grid is selected to match the scanning geometry, translational and rotational scanning symmetries as well as axial symmetries of the transducer surface can be considered to build the model matrix [75–77]. In this manner, the $p_i(r,t)$ signals for all positions can be derived from that corresponding to a reference position. This facilitates storage of the model matrix in memory, which if often challenging, particularly for three-dimensional imaging.

3 The inverse problem

The OA forward model enables calculating the theoretical pressure (or transducer) signals as a linear function of the initial pressure distribution (sources). MB OA image reconstruction corresponds to the inverse problem aiming at estimating the initial pressure rise from the acquired signals. This is generally formulated as an optimization-based problem involving minimizing the energy functional defined as

$$\mathbf{p}_{0,sol} = \underset{\mathbf{p}_0\ (\geq 0)}{\operatorname{argmin}} \left\{ \left\| \mathbf{p}_m - \mathbf{A}\mathbf{p}_0 \right\|_2 + \lambda R(\mathbf{p}_0) \right\}, \tag{5}$$

where $\mathbf{p}_m$ are the measured signals expressed in a vector form. The first term of Eq. 5 corresponds to the data fidelity term driving the solution towards the observed data. $R(\mathbf{p}_0)$ corresponds to the regularization term, being λ the regularization parameter. Optionally, $\mathbf{p}_0$ can be constrained e.g. not to have negative values ($\mathbf{p}_0 \geq 0$) in order to avoid solutions with no physical meaning [57]. Regularization is generally included in the inversion problem to reduce the effects of noise and data incompleteness and/or to incorporate prior knowledge on the image. The simplest and most standard regularization strategy to stabilize the inversion, known as Tikhonov regularization, is based on the L2 norm of the image, i.e., $R(\mathbf{p}_0) = \|\mathbf{p}_0\|_2$. In this case, the unconstrained solution of Eq. 5 is analytically expressed as

$$\mathbf{p}_{0,sol} = \left(\mathbf{A}^T\mathbf{A} + \lambda\mathbf{I}\right)^{-1}\mathbf{A}^T\mathbf{p}_m, \tag{6}$$

being $\mathbf{A}^T$ the transpose of the model matrix. Note, however, that Eq. 6 is impractical in most cases due to the large size of the model matrix, particularly for high-resolution three-dimensional imaging. Thereby, the inversion problem in Eq. 5 is solved iteratively e.g. with algorithms based on steepest descent or conjugate gradient methods [58]. The matrix-vector multiplications involving the model matrix and its transpose are the most computationally demanding operations in iterative algorithms. In some cases, the model matrix cannot be stored in memory and the elements of the model matrix are calculated in each iteration to perform these operations. Graphics processing unit (GPU)-based parallelization of these operations is then essential to accelerate the inversion process. For this, efficient methods for on-the-fly calculation of the elements of the model matrix e.g. based on look-up tables are needed, since GPU-storage of the entire matrix is generally not possible [55, 74].

If a very large regularization term (strong Tikhonov regularization) is chosen to suppress artifacts and enhance signal-to-noise ratio (SNR), the term $\lambda\mathbf{I}$ becomes dominant over $\mathbf{A}^T\mathbf{A}$, thus in Eq. 6 can be approximated as

$$\mathbf{p}_{0,sol} = \mathbf{A}^T\mathbf{p}_m. \tag{7}$$

$\mathbf{A}^T$ is the algebraic adjoint (transpose) of the discrete-to-discrete OA forward model. The adjoint of the continuous operator can also be calculated prior to discretization, which enables exploiting fast wave propagation solvers [78]. Equation 7 can be interpreted as a model back-projection (MBP, non-iterative) reconstruction approach associated to the discrete-to-discrete model and enabling fast reconstructions. It can also be regarded as a cross-correlation with the theoretical signals generated by each voxel and can be interpreted in terms of a matched filter [79].

4 Outperforming filtered back-projection

MB (iterative) reconstruction methods were used to reconstruct the first x-ray CT images. However, they were quickly replaced by less complex FBP algorithms and were not implemented in commercial scanners until around 10 years ago [80]. The wide use of FBP algorithms in x-ray CT fostered the development of similar formulas for OA tomography [41, 42, 81, 82] whose discretized versions are still in common use. Particularly, GPU-based implementations of FBP algorithms enable real-time preview of three-dimensional data, which is essential for the clinical translation of the OA technology [83].

Sparse spatial sampling of signals is common in OA tomography since transducer arrays are routinely used for real-time imaging [84]. Indeed, *ad-hoc* design of US arrays with optimized OA performance generally focuses on increasing the angular coverage to avoid limited-view effects rather than on reducing the inter-element pitch [85]. Much like in x-ray CT, reduced spatial sampling is known to result in streak-type artefacts in the images. These artefacts, illustrated in Figure 2A, are a consequence of signals from strong absorbers such as blood vessels being back-projected into arcs, which average out for a sufficient number of measuring locations but can lead to strong noise in the images if the number of collected signals is relatively small. The capability of MB OA algorithms to mitigate this and other sources of noise has been demonstrated with the development of the first iterative algorithms [46]. Figure 2B shows an example of a cross-sectional MB algorithm significantly reducing the noise in the OA images of the mouse brain with respect to those obtained with FBP [86]. Iterative MB reconstruction could also clearly enhance the performance of full-body three-dimensional small-animal imaging systems [48]. In the example shown in Figure 2C, OA images reconstructed with FBP are clearly afflicted by noise even though a large number of signals (11,520) were used for reconstruction. The noise could be reduced by considering an optimization-based framework including a total-variation (TV) regularization term, i.e., $R(\mathbf{p}_0) = \| \sqrt{(\frac{\partial \mathbf{p}_0}{\partial x})^2 + (\frac{\partial \mathbf{p}_0}{\partial y})^2 + (\frac{\partial \mathbf{p}_0}{\partial z})^2} \|_1$. The effects of streak-type artefacts in three-dimensional OA images are more prominent if these are acquired with hand-held scanners based on spherical arrays, currently being used in clinical trials [87, 88]. Indeed, even though three-dimensional imaging is possible with a single laser pulse, the number of signals that can be simultaneously collected with an array is generally significantly lower than that required according to the Nyquist spatial sampling criterion [89]. Figure 2D shows an example of an image of the finger vasculature of a healthy volunteer [55]. The MBP approach (Eq. 7) is shown to reduce the background noise of FBP images, while still begin able to

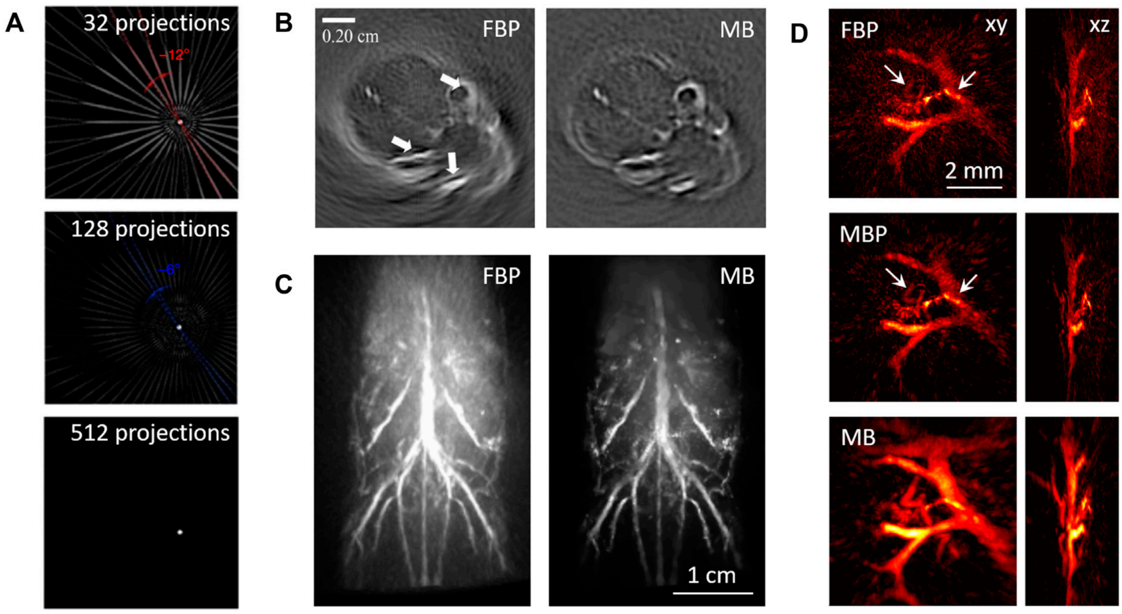

FIGURE 2
Performance comparison of model-based (MB) and filtered back-projection (FBP). **(A)** Example of streak-type artefacts produced in the reconstructed images as a function of the number of sensors considered. Adapted from [171] with permission from Nature Publishing Group. **(B)** Comparison of the cross-sectional images of the mouse brain rendered with FBP and MB. Adapted from [86] with permission from American Institute of Physics. **(C)** Comparison of the three-dimensional full-wave images reconstructed with FBP and MB based on total-variation regularization. Adapted from [48] with permission from Institute of Physics. **(D)** Comparison of the three-dimensional images of the finger vasculature of a healthy volunteer obtained with FBP, model back-projection (MBP) and MB based on Tikhonov regularization. Reprinted from [55] with permission from Institute of Electrical and Electronics Engineers.

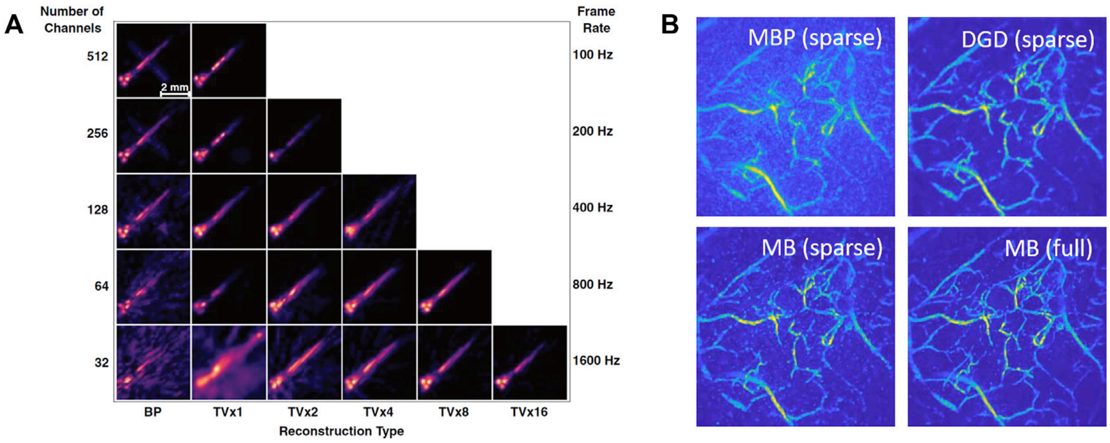

FIGURE 3
Model-based (MB) reconstruction from sparse data based on advanced regularization methods. **(A)** Performance of three-dimensional MB reconstruction based on total-variation (TV) regularization in the spatial and temporal domains. As a reference, the images reconstructed with filtered back-projection (FBP) are shown in the left column as a function of the number of time-resolved signals considered. The equivalent MB images are shown in the other columns. TVxN indicates that a sequence of N images is simultaneously reconstructed. Reprinted from [99] with permission from Optica Publishing Group. **(B)** Performance of the deep gradient descent (DGD) algorithm when considering signals sub-sampled by a factor of 4 in the spatial and temporal domains. The image obtained with DGD after 5 iterations (top right) is compared to the image obtained with the model back-projection (MBP) method (1 iteration, top left) and iterative TV-based MB algorithm (20 iterations, bottom left). As a reference, the image reconstructed with the same TV-based MB algorithm (20 iterations) from the full data is also shown (bottom right). Adapted from [101] with permission from Institute of Electrical and Electronics Engineers.

provide real-time feed-back during the scans. Iterative MB inversion based on Tikhonov regularization clearly provides an enhanced imaging performance, but results in a longer computation time in the order of 5 s.

MB reconstruction is more flexible than FBP as it is generally applicable regardless of the acquisition geometry. Moreover, it facilitates guiding the solution towards an image consistent with prior knowledge on the sample. For example, the images reconstructed with FBP are known to be affected by negative values with no negative meaning [90]. These can be avoided by including non-negative constraints in the optimization-based framework [57, 91, 92]. The regularization term in the energy functional to be minimized (Eq. 5) also plays an essential role in the contrast, resolution and overall quality of the image being rendered. For example, an L1-based regularization term in the image domain, i.e., $R(\mathbf{p_0}) = \|\mathbf{p_0}\|_1$, tends to set many voxels to zero (or close to zero) values. This was exploited to enhance the spatial resolution beyond the acoustic diffraction barrier [76, 92, 93]. TV-based regularization is also commonly used as it enables mitigating noise while preserving sharp edges [52, 53, 94–98]. Figure 3A displays a comparison of the images of a freely-swimming zebrafish larvae reconstructed with FBP and MB including a TV regularization term in the spatial and temporal domains, i.e., $R(\mathbf{p_0}) = \|\sqrt{(\frac{\partial \mathbf{p_0}}{\partial x})^2 + (\frac{\partial \mathbf{p_0}}{\partial y})^2 + (\frac{\partial \mathbf{p_0}}{\partial z})^2 + k(\frac{\partial \mathbf{p_0}}{\partial t})^2}\|_1$. A sequence of images is simultaneously reconstructed with this approach following a sparse acquisition scheme [99]. MB reconstruction then enables significantly reducing the required number of signals for each laser pulse and thus increasing the achievable frame rate [100].

Defining the optimal regularization strategy is generally challenging as prior information may not be available and/or cannot be expressed by standard regularization terms. Also, regularizers known to provide a good performance in other imaging modalities may be suboptimal for OA. The MB performance can be enhanced by learning realistic information on the expected image content and how to best incorporate this in an iterative reconstruction approach. For this, convolutional neural networks have been suggested. These can be used e.g. to iteratively update the reconstructed OA image from the previous image and the gradient of the fidelity term [101]. The regularization effects are then learned from the data during training. The performance of this reconstruction approach, termed deep gradient descent (DGD), is shown in Figure 3B when using x-ray CT angiography images for training. The updated image after 5 iterations of the DGD method considering data sub-sampled by a factor of 4 is shown to clearly reduce the noise of the MBP image, corresponding to the first iteration (Figure 3B, top). The DGD can also provide more accurate results than standard iterative MB reconstruction based on TV regularization for the same data sparsity level (Figure 3B, bottom left), as validated with the equivalent TV-based image reconstructed from the full data (Figure 3B, bottom right).

5 Modelling the transducer response

FBP formulas are derived by considering the spatio-temporal pressure wavefield at a surface surrounding the sample. As mentioned above, OA signals are often acquired at a relatively sparse distribution of measuring locations. Also, standard piezoelectric US transducers have a finite size and a finite detection bandwidth, thus the collected signals generally differ from the acoustic pressure.

The effects of the transducer are generally characterized as a convolution with the so-called electrical impulse response (EIR) and the spatial impulse response (SIR). The EIR corresponds to the signal for an impulse-type wavefront incident normal to the surface of the transducer [102]. The SIR is associated to the finite aperture of the transducer and has long been known to degrade the tangential resolution in the reconstructed OA images [72, 103]. Both the EIR and the SIR can be incorporated into a MB reconstruction framework. As an example, Figure 4A displays the OA images reconstructed with the simulated signals for a flat transducer with 6 mm diameter circularly scanned around the sample with 50 mm radius [103]. Point absorbers at distances of up to 25 mm away from the scanning center could be accurately reconstructed with a MB algorithm accounting for the SIR, while the OA images reconstructed with FBP clearly show a progressive reduction in the azimuthal resolution at peripheral regions. For a finite-size transducer perfectly matched to the acoustic coupling medium, the SIR is approximated as the integral of the pressure on the active surface [104]. This enables estimating analytically the SIR of some types of sensors [72, 105]. Alternatively, the active surface of the sensor can be numerically approximated to estimate the SIR [47, 73, 106]. Figure 4B shows the OA microscopy images of the subcutaneous murine vasculature obtained with a broadband spherical polyvinylidene difluoride (PVDF) transducer [76]. A MB algorithm incorporating the SIR clearly outperformed a back-projection-based synthetic aperture focusing technique (SAFT). Specifically, the vascular network at different depths was more clearly resolved with the MB considering a L2-norm-based regularization term. Also, an increase in resolution beyond the barrier of acoustic diffraction was achieved with L1-norm-based regularization to the detriment of the number of vascular branches being observed. A similar enhanced performance was observed with MB reconstruction in other acquisition geometries [55, 107–110], which substantiates the general applicability of this approach. It is important to note that the estimated SIR is based on an approximation. Wave propagation and energy conversion within piezoelectric materials is generally more complex. A more accurate estimation of the spatially-dependent total impulse response (TIR) of the transducer can be performed

10.3389/fphy.2022.1028258

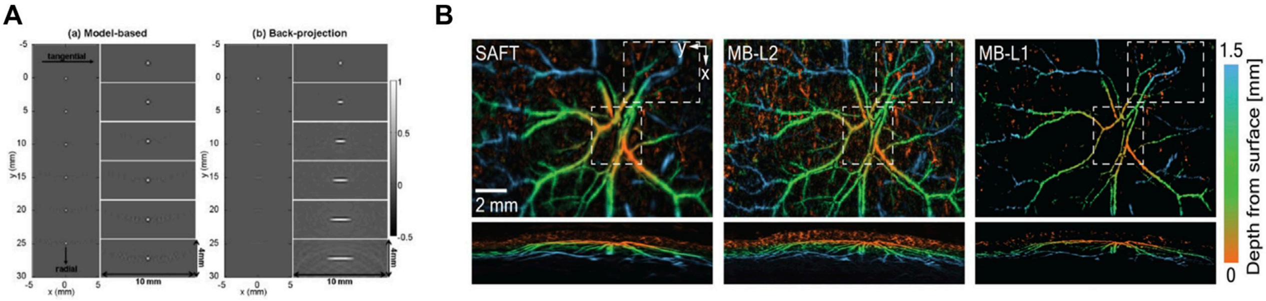

FIGURE 4
Accounting for the finite aperture of the ultrasound transducer. **(A)** Comparison of the optoacoustic (OA) images reconstructed with MB and filtered back-projection (FBP) algorithms considering the simulated signals for a flat transducer circularly scanned around the sample. Reprinted from [103] with permission from Optica Publishing Group. **(B)** Comparison of the OA microscopy images of the subcutaneous murine vasculature obtained with a FBP-based synthetic aperture focusing technique (SAFT, left), a MB algorithm considering a L2-norm regularization term (middle) and a MB algorithm considering a L1-norm regularization term (right). Reprinted from [76] with permission from Wiley Online Library.

by scanning a sub-resolution absorber [111, 112]. The TIR can then be incorporated into the MB reconstruction framework to further enhance the reconstruction accuracy [113]. The TIR may also be measured by considering the response of small particles flowing in blood [114–116], which may facilitate enhancing the imaging performance *in vivo*.

6 Accounting for acoustic propagation effects

Direct inversion of a Radon-type transform into a FBP formula is only possible for a uniform non-attenuating acoustic medium. However, biological tissues are heterogeneous acoustic media further absorbing part of the acoustic energy. In soft tissues, the speed of sound can change within a range of approximately ±10% [117]. This mainly affects the time-of-flight of US waves, which results in a time-shift of the collected signals [118]. Other effects such as reflections, refractions or scattering can further result in strong artefacts in the images [119–121], but these are only prominent in other tissues featuring stronger acoustic mismatch such as bones or lungs. On the other hand, frequency-dependent acoustic attenuation causes both a decrease in intensity and a reduction in bandwidth of the collected signals, which in turn results in quantification errors and in a loss of spatial resolution [122, 123].

MB reconstruction frameworks provide a flexible means for compensating for all these effects. For uniform non-attenuating acoustic media, discrete-to-discrete time-domain OA forward models can be built by discretizing the Poisson-type integral corresponding to the solution of Eq. 1 [68]. The effects of speed of sound changes can then be corrected by modifying the integration surface (or curve) based on the induced time-of-flight changes [49]. Full-wave MB algorithms based on the exact OA wave equation have also been suggested to mitigate the effects of speed of sound heterogeneities [33, 78, 124, 125]. Also, so-called joint-reconstruction MB algorithms aiming at simultaneously recovering an OA image and the speed of sound distribution have been suggested [126, 127]. These algorithms were shown to be ill-conditioned and numerically unstable [128], but could be used to reconstruct cross-sectional images of mice by considering a low-dimensional parametrization of the sound speed distribution [129]. MB algorithms can also be used to reconstruct the speed of sound distribution from transmitted US waves [130]. Figure 5A shows a comparison of the OA images of the murine liver region obtained with MB algorithms assuming a uniform speed of sound and considering two different speed of sound values for the tissue and coupling medium, respectively [129]. TV regularization was used in both cases. The distortion induced in the images due to speed of sound changes is higher when using heavy water as coupling medium [131] or air-coupled transducers [132, 133]. Acoustic attenuation effects can also be accounted for with MB algorithms. These correspond to a convolution of the time-domain signals (columns of the model matrix) with an attenuation impulse response function [123]. Recently, cross-sectional OA tomography based on a full-ring array was combined with transmission US methods providing speed of sound and attenuation maps [134]. This information can then be exploited in MB reconstruction frameworks to advance the OA imaging performance. In principle, full-wave MB algorithms can account for any effect associated to acoustic propagation in strongly mismatched tissues. However, this approach is impractical unless accurate knowledge of the distribution of acoustic properties is available. The artefacts induced in the images can be mitigated by weighting the signals and the model matrix so that less distorted signals have a higher influence in the inversion algorithm [135]. This approach was initially suggested for FBP algorithms [136, 137].

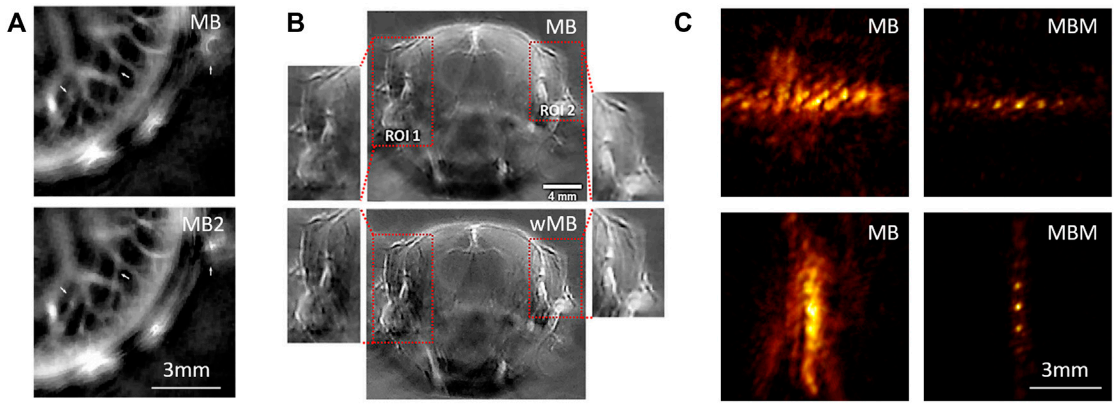

FIGURE 5
Accounting for acoustic heterogeneities in the sample. **(A)** Comparison of the cross-sectional optoacoustic (OA) images of the mouse liver reconstructed with a model-based (MB) algorithm considering a uniform speed of sound (top) and a MB algorithm considering a different speed of sound within the mouse and the water coupling medium (MB2, bottom). Adapted from [129] with permission from Society for Industrial and Applied Mathematics. **(B)** Comparison of the cross-sectional OA images of the mouse brain reconstructed with a standard MB algorithm (top) and a MB algorithm weighted with the probability the collected signals are distorted by scattering or reflection events (wMB, bottom). Reprinted from [138] with permission from Wiley Online Library. **(C)** Transcranial OA images reconstructed with a standard MB algorithm (left) and with a MB algorithm built from a reference signal based on the OA memory effect (MBM, right) [142].

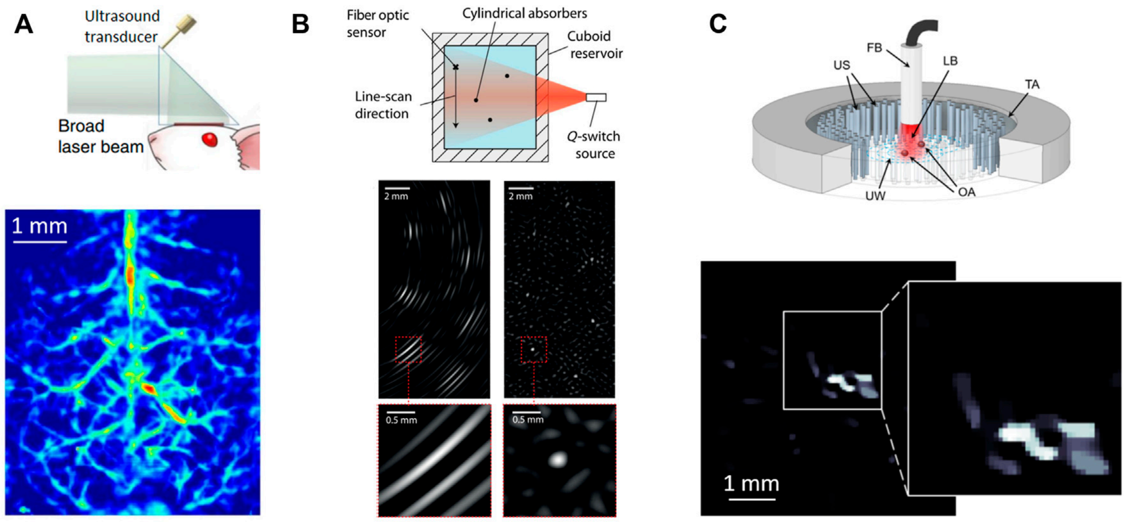

FIGURE 6
Model-based (MB) image reconstruction with time-resolved optoacoustic (OA) signals encoding the position of absorbers *via* complex propagation of ultrasound (US) waves. **(A)** Image of the cortical vasculature of the mouse brain obtained by exploiting US propagation through an ergodic relay. Adapted from [150] with permission from Nature Publishing Group. **(B)** Image of seven synthetic hairs sparsely distributed within an acoustically reverberant cavity causing multiple reflections of the US waves. Reprinted from [151] with permission from Optica Publishing Group. **(C)** Image of a zebrafish larva obtained by exploiting US transmission through a randomized scattering medium. Adapted from [71] with permission from American Physical Society.

Figure 5B shows a comparison of the coronal cross-sectional OA images of the mouse brain reconstructed with a standard MB algorithm and with a weighted MB (wMB) algorithm considering the probability that the signals are distorted by scattering events [138], indicating the enhanced performance achieved with the latter. Arguably, the greatest challenge in OA is to achieve high-resolution imaging through the skull bone, particularly in humans. Transcranial US propagation is known to be affected by reflections, refractions, mode conversion and other effects [139, 140]. OA forward models accounting for some of these effects have been suggested [141], but their applicability *in vivo* is challenged by the lack of accurate knowledge on cranial acoustic and dimensional properties. Recently, it has been demonstrated that the distortion of optoacoustically-generated waves is locally preserved after transcranial propagation [142]. A MB reconstruction algorithm can then be developed based on this memory effect (MBM). Figure 5C shows the enhanced performance achieved with the MBM algorithm with respect to a standard MB algorithm assuming a uniform speed of sound. The strong distortion induced by the skull is clear in the MB-reconstructed images, while high-resolution images of point absorbers could be obtained with the MBM algorithm.

7 Compressed acquisition and reconstruction

MB frameworks are also particularly suitable for recovering signals or images from a few signal samples in the spatial and/or temporal dimensions. Mathematically, this corresponds to finding a solution of an underdetermined linear system and is the basis of compressed sensing methods [143]. Efficient recovery implies two conditions, namely that the signal (or image) exhibits sparsity in some domain and that the sampling matrix verifies the so-called restricted isometry property. The lack of speckle noise in OA images promotes sparsity, thus facilitates defining compressed acquisition and reconstruction schemes.

Compressed-sensing-based methods have been widely used in OA for reconstructing images from so-called partial data [50, 144–147]. Generally, this corresponds to signal acquisition at a spatially sparse location of sensors. Note that this is fundamentally different than the limited-view problem. Indeed, signals acquired under limited-view conditions lack sufficient information to achieve accurate OA reconstructions regardless the spatial and temporal sampling density [36]. An approach to recover information from partial data consists in formulating a MB problem to reconstruct the OA signals corresponding to dense spatial sampling and subsequently perform image reconstruction [83]. Alternatively, MB image reconstruction capitalizing on compressed-sensing principles can be performed, which generally implies L1-norm-based regularization terms [50, 144–146, 148, 149]. It is important to take into account that the advantage of sparse sampling is two-fold. On the one hand, compressed data acquisition significantly reduces the complexity of the transducer array and associated electronics, thus facilitates the development of low-cost OA imaging systems. On the other hand, the imaging rate can be significantly accelerated for a given data throughput capacity. Recently, OA imaging with a single time-resolved signal has been achieved by encoding the location of absorbers *via* complex propagation of the generated US waves. Three examples of systems based on this principle are shown in Figure 6. Figure 6A shows the OA images of the cortical murine vasculature reconstructed by considering the time-resolved signal acquired with a single-element transducer and single-shot excitation [150]. For this, US wave propagation through an ergodic relay causing multiple reflections was exploited. The model-matrix was experimentally calibrated by scanning a focused laser beam. Figure 6B shows the image seven sparsely-distributed synthetic hairs obtained with a different system based on a reverberant cavity also causing multiple reflections of US [151]. In this case, the signal from an individual synthetic hair was used for calibration. Figure 6C displays the image of a zebrafish larva obtained by exploiting acoustic scattering to physically encode the position of optical absorbers in the acquired signals [71]. For this, an imaging system based on ultrasound propagation through a randomized scattering medium was used. The model-matrix was experimentally calibrated by scanning an individual absorbing microsphere.

8 Summary and outlook

In this article, we described the basis of both iterative and non-iterative MB reconstructions in OA imaging and reviewed recent work on this topic. The reported results, based on OA models independently developed by different groups, have systematically demonstrated an enhanced performance with respect to conventional reconstruction methods. In particular, the commonly-used FBP algorithms are often afflicted by noise and other artefacts, even when considering an arrangement of sensors for which an accurate FBP formula - derived from the inversion of a Radon-type transform - is available. Iterative methods provide a flexible means for mitigating these artefacts, further rendering a solution consistent with *a priori* knowledge on the sample. This is achieved by properly selecting regularization terms, constraints or number of iterations. Moreover, the spatial- and frequency-dependent response of the US transducer(s) as well as acoustic heterogeneities and attenuation can be accurately accounted for with MB methods. In this manner, it was possible to advance the OA imaging capabilities to a new level of performance e.g. by enabling breaking through the resolution limit dictated by acoustic diffraction. Considering the large variety of existing OA embodiments and the fact that the OA hardware is continuously being upgraded, new MB methods can be developed or adapted to new systems. Thereby, further research on MB reconstruction is expected.

The existence of a linear OA forward model stems from the thermoelastic generation mechanism of US within biological tissues, regardless the complexity of the acoustic media or the type and arrangement of US sensors [152]. We have shown that mathematical modelling of this effect results in a well-defined source term in the time-domain wave equation corresponding to short-pulsed excitation. Similarly, wave equations in the time or frequency domains can be derived for other types of time-varying light sources [153]. This is fundamentally different from pulse-echo US or other coherent imaging modalities based on back-scattered waves from different types of sources. For homogenous media, a solution of the wave equation exists and a discrete OA forward model, defined as a model matrix, can be theoretically derived from it. However, analytical derivation of the forward model is significantly more challenging when considering the propagation of US waves through complex media or through piezoelectric sensing materials. In this case, the model-matrix can be experimentally calibrated by collecting the OA signals generated by sub-resolution optical absorbers at a grid of points covering the region of interest. The number of signals required for experimentally building the model-matrix can be significantly reduced by considering the OA memory effect if the isoplanatic zone is relatively large due to symmetries in the scanning geometry [154]. Indeed, MB reconstruction based on an experimentally calibrated matrix enabled exploiting the complex propagation of US waves to encode the absorption distribution in a single OA signal or imaging through strongly mismatch acoustic media such as the skull bone.

MB methods are also commonly used for linear un-mixing of spectrally-distinctive chromophores such as oxygenated and deoxygenated haemoglobin from OA images acquired at multiple wavelengths [155, 156]. Multi-spectral (multi-wavelength) OA imaging is a powerful approach for molecular imaging applications provided accurate quantification of the bio-distribution of specific molecules is achieved [4, 5, 23, 157–159]. The combination of reconstruction and un-mixing steps into a single model-matrix has been shown to render more quantitative results if regularization parameters and non-negative constraints are properly selected [160]. Also, the model-matrix can incorporate the wavelength-dependent light fluence distribution within the sample, which can be estimated with different methods [161–165]. Thereby, the so-called spectral coloring effects, which hamper quantification of tissue oxygenation, can potentially be mitigated [156].

In recent years, deep learning has rapidly emerged as an appealing alternative for tomographic image reconstruction and processing. MB methods are sometimes categorized as knowledge-driven as they are based on minimizing the error between estimations of a physical model and actual data. On the contrary, deep learning methods are based on "reconstructing" the inversion model by minimizing the error between predicted and ground truth data. This data driven approach has similarities with experimentally-calibrated MB methods but the computationally efficiency can greatly be enhanced once the network has been trained. However, the ways deep neural networks process data are mathematically not fully understood with serious concerns raised regarding validity of the results. Nevertheless, in the OA field deep learning has been used for image quality improvement as well as for directly reconstructing images from the acquired signals [166–179]. Also, it was possible to train neural networks to learn the regularization term in an iterative MB inversion framework [101, 180, 181]. The latter hybrid method combines the advantages of both approaches further highlighting the importance of physical modeling for enhancing reliability and practical applicability of newly developed neural networks. The regularization performance in this case depends on the data quality as well as on the amount of data used for training. Combination of MB and deep learning methods is expected to emerge as a promising research direction.

In summary, MB reconstruction is a powerful tool for enhancing image quality and performance of OA imaging systems. Its efficacy derives from accurate physical modelling of US generation and propagation further accounting for experimental imperfections and other effects using either mathematical derivations or experimental calibrations. It has been demonstrated that MB approaches may facilitate super-resolution imaging, accurate image reconstruction from partial data as well as imaging through strongly aberrative media. The MB framework can further be exploited for processing multi-spectral or time-lapse data. Performance of MB approaches can be enhanced by incorporating neural networks, e.g. to act as regularizers.

Author contributions

XLD-B and DR wrote the manuscript.

Acknowledgments

XLD-B acknowledges funding support from the Helmut Horten Stiftung.

Conflict of interest

The authors declare that the research was conducted in the absence of any commercial or financial relationships that could be construed as a potential conflict of interest.

Publisher's note

References

1. Zeng GL. *Medical image reconstruction: A conceptual tutorial*. Springer (2010).

2. Ravishankar S, Ye JC, Fessler JA. Image reconstruction: From sparsity to data-adaptive methods and machine learning. *Proc IEEE* (2019) 108(1):86–109. doi:10.1109/jproc.2019.2936204

3. McCann MT, Unser M. Biomedical image reconstruction: From the foundations to deep neural networks. *FNT Signal Process.* (2019) 13(3):283–357. doi:10.1561/2000000101

4. Deán-Ben X, Gottschalk S, Mc Larney B, Shoham S, Razansky D. Advanced optoacoustic methods for multiscale imaging of *in vivo* dynamics. *Chem Soc Rev* (2017) 46(8):2158–98. doi:10.1039/c6cs00765a

5. Yao J, Wang LV. Recent progress in photoacoustic molecular imaging. *Curr Opin Chem Biol* (2018) 45:104–12. doi:10.1016/j.cbpa.2018.03.016

6. Manohar S, Gambhir S. *Photoacoustics* (2020) 19.

7. Omar M, Aguirre J, Ntziachristos V. Optoacoustic mesoscopy for biomedicine. *Nat Biomed Eng* (2019) 3(5):354–70. doi:10.1038/s41551-019-0377-4

8. Ni R, Chen Z, Deán-Ben XL, Voigt FF, Kirschenbaum D, Shi G, et al. *Nat Biomed Eng* (2022) 1–14.

9. Wissmeyer G, Pleitez MA, Rosenthal A, Ntziachristos V. *Light: Sci Appl* (2018) 7(1):1–16.

10. Cho S-W, Park SM, Park B, Lee TG, Kim B-M, Kim C, et al. High-speed photoacoustic microscopy: A review dedicated on light sources. *Photoacoustics* (2021) 24:100291. doi:10.1016/j.pacs.2021.100291

11. Manwar R, Kratkiewicz K, Avanaki K. Overview of ultrasound detection technologies for photoacoustic imaging. *Micromachines* (2020) 11(7):692. doi:10.3390/mi11070692

12. Chen Z, Özbek A, Rebling J, Zhou Q, Deán-Ben XL, Razansky D. Multifocal structured illumination optoacoustic microscopy. *Light Sci Appl* (2020) 9(1):152–9. doi:10.1038/s41377-020-00390-9

13. Deán-Ben XL, Sela G, Lauri A, Kneipp M, Ntziachristos V, Westmeyer GG, et al. Functional optoacoustic neuro-tomography for scalable whole-brain monitoring of calcium indicators. *Light Sci Appl* (2016) 5(12):e16201. doi:10.1038/lsa.2016.201

14. Guggenheim JA, Zhang EZ, Beard PC. A method for measuring the directional response of ultrasound receivers in the range 0.3–80 MHz using a laser-generated ultrasound source. *IEEE Trans Ultrason Ferroelectr Freq Control* (2017) 64(12):1857–63. doi:10.1109/tuffc.2017.2758173

15. Kurnikov A, Pavlova K, Orlova AG, Khilov AV, Perekatova V, Kovalchuk A, et al. Broadband (100 kHz – 100 MHz) ultrasound PVDF detectors for raster-scan optoacoustic angiography with acoustic resolution. *Quan Elec (Woodbury)* (2021) 51(5):383–8. doi:10.1070/qel17538

16. Deán-Ben XL, Razansky D. Optoacoustic imaging of the skin. *Exp Dermatol* (2021) 30(11):1598–609. doi:10.1111/exd.14386

17. Schellenberg MW, Hunt HK. Hand-held optoacoustic imaging: A review. *Photoacoustics* (2018) 11:14–27. doi:10.1016/j.pacs.2018.07.001

18. Ron A, Deán-Ben XL, Gottschalk S, Razansky D. Volumetric optoacoustic imaging unveils high-resolution patterns of acute and cyclic hypoxia in a murine model of breast cancer. *Cancer Res* (2019) 79(18):4767–75. doi:10.1158/0008-5472.can-18-3769

19. Na S, Russin JJ, Lin L, Yuan X, Hu P, Jann KB, et al. Massively parallel functional photoacoustic computed tomography of the human brain. *Nat Biomed Eng* (2022) 6(5):584–92. doi:10.1038/s41551-021-00735-8

20. Li Y, Lu G, Zhou Q, Chen Z. Advances in endoscopic photoacoustic imaging. *Photonics* (2021) 8(7):281. doi:10.3390/photonics8070281

21. Kalva SK, Dean-Ben XL, Razansky D. Single-sweep volumetric optoacoustic tomography of whole mice. *Photon Res* (2021) 9(6):899–908. doi:10.1364/prj.418591

22. Zheng W, Huang C, Zhang H, Xia J. *Biomed Eng Lett* (2022) 1–9.

23. Weber J, Beard PC, Bohndiek SE. Contrast agents for molecular photoacoustic imaging. *Nat Methods* (2016) 13(8):639–50. doi:10.1038/nmeth.3929

24. Liu W, Yao J. Photoacoustic microscopy: Principles and biomedical applications. *Biomed Eng Lett* (2018) 8(2):203–13. doi:10.1007/s13534-018-0067-2

25. Merčep E, Deán-Ben XL, Razansky D. Imaging of blood flow and oxygen state with a multi-segment optoacoustic ultrasound array. *Photoacoustics* (2018) 10:48–53. doi:10.1016/j.pacs.2018.04.002

26. Balasundaram G, Ding L, Li X, Attia ABE, Dean-Ben XL, Ho CJH, et al. Noninvasive anatomical and functional imaging of orthotopic glioblastoma development and therapy using multispectral optoacoustic tomography. *Translational Oncol* (2018) 11(5):1251–8. doi:10.1016/j.tranon.2018.07.001

27. Lafci B, Merčep E, Herraiz JL, Deán-Ben XL, Razansky D. Noninvasive multiparametric characterization of mammary tumors with transmission-reflection optoacoustic ultrasound. *Neoplasia* (2020) 22(12):770–7. doi:10.1016/j.neo.2020.10.008

28. Kalva SK, Sánchez-Iglesias A, Deán-Ben XL, Liz-Marzán LM, Razansky D. Rapid volumetric optoacoustic tracking of nanoparticle kinetics across murine organs. *ACS Appl Mater Inter* (2021) 14(1):172–8. doi:10.1021/acsami.1c17661

29. Wang LV, Yao J. A practical guide to photoacoustic tomography in the life sciences. *Nat Methods* (2016) 13(8):627–38. doi:10.1038/nmeth.3925

30. Treeby BE, Cox BT. k-Wave: MATLAB toolbox for the simulation and reconstruction of photoacoustic wave fields. *J Biomed Opt* (2010) 15(2):021314. doi:10.1117/1.3360308

31. Rosenthal A, Ntziachristos V, Razansky D. Acoustic inversion in optoacoustic tomography: A review. *Curr Med Imaging Rev* (2013) 9(4):318–36. doi:10.2174/15734056113096660006

32. Deán-Ben XL, Razansky D. Optoacoustic image formation approaches—A clinical perspective. *Phys Med Biol* (2019) 64(18):18TR01. doi:10.1088/1361-6560/ab3522

33. Wang T, Liu W, Tian C. Combating acoustic heterogeneity in photoacoustic computed tomography: A review. *J Innov Opt Health Sci* (2020) 13(03):2030007. doi:10.1142/s1793545820300074

34. Bohndiek S. Addressing photoacoustics standards. *Nat Photon* (2019) 13(5):298. doi:10.1038/s41566-019-0417-3

35. Xu Y, Wang LV, Ambartsoumian G, Kuchment P. Reconstructions in limited-view thermoacoustic tomography. *Med Phys* (2004) 31(4):724–33. doi:10.1118/1.1644531

36. Deán-Ben XL, Razansky D. On the link between the speckle free nature of optoacoustics and visibility of structures in limited-view tomography. *Photoacoustics* (2016) 4(4):133–40. doi:10.1016/j.pacs.2016.10.001

37. Lu T, Chen T, Gao F, Sun B, Ntziachristos V, Li J. LV-GAN: A deep learning approach for limited-view optoacoustic imaging based on hybrid datasets. *J Biophotonics* (2021) 14(2):e202000325. doi:10.1002/jbio.202000325

38. Paltauf G, Nuster R, Haltmeier M, Burgholzer P. Experimental evaluation of reconstruction algorithms for limited view photoacoustic tomography with line detectors. *Inverse Probl* (2007) 23(6):S81–94. doi:10.1088/0266-5611/23/6/s07

39. Dean-Ben XL, Buehler A, Ntziachristos V, Razansky D. Accurate model-based reconstruction algorithm for three-dimensional optoacoustic tomography. *IEEE Trans Med Imaging* (2012) 31(10):1922–8. doi:10.1109/tmi.2012.2208471

40. Moon S. Inversion formula for a radon-type transform arising in photoacoustic tomography with circular integrating detectors. *Adv Math Phys* (2018) 2018:1–4. doi:10.1155/2018/1727582

41. Xu M, Wang LV. Universal back-projection algorithm for photoacoustic computed tomography. *Phys Rev E* (2005) 71(1):016706. doi:10.1103/physreve.71.016706

42. Burgholzer P, Bauer-Marschallinger J, Grün H, Haltmeier M, Paltauf G. Temporal back-projection algorithms for photoacoustic tomography with integrating line detectors. *Inverse Probl* (2007) 23(6):S65–80. doi:10.1088/0266-5611/23/6/s06

43. Ozbek A, Deán-Ben X, Razansky D. Realtime parallel back-projection algorithm for three-dimensional optoacoustic imaging devices. In: European conference on biomedical optics. Washington, DC: Optica Publishing Group (2013). p. 88000I.

44. Deán-Ben XL, Ozbek A, Razansky D. Volumetric real-time tracking of peripheral human vasculature with GPU-accelerated three-dimensional optoacoustic tomography. *IEEE Trans Med Imaging* (2013) 32(11):2050–5. doi:10.1109/tmi.2013.2272079

45. Defrise M, Gullberg GT. Image reconstruction. *Phys Med Biol* (2006) 51(13):R139–54. doi:10.1088/0031-9155/51/13/r09

46. Paltauf G, Viator J, Prahl S, Jacques S. Iterative reconstruction algorithm for optoacoustic imaging. *The J Acoust Soc America* (2002) 112(4):1536–44. doi:10.1121/1.1501898

47. Caballero MAA, Gateau J, Déan-Ben X-L, Ntziachristos V. *IEEE Trans Med Imaging* (2013) 33(2):433–43.

48. Wang K, Su R, Oraevsky AA, Anastasio MA. Investigation of iterative image reconstruction in three-dimensional optoacoustic tomography. *Phys Med Biol* (2012) 57(17):5399–423. doi:10.1088/0031-9155/57/17/5399

49. Dean-Ben XL, Ntziachristos V, Razansky D. Acceleration of optoacoustic model-based reconstruction using angular image discretization. *IEEE Trans Med Imaging* (2012) 31(5):1154–62. doi:10.1109/tmi.2012.2187460

50. Arridge S, Beard P, Betcke M, Cox B, Huynh N, Lucka F, et al. Accelerated high-resolution photoacoustic tomography via compressed sensing. *Phys Med Biol* (2016) 61(24):8908–40. doi:10.1088/1361-6560/61/24/8908

51. De Cezaro A, De Cezaro FT, Suarez JS. Regularization approaches for quantitative Photoacoustic tomography using the radiative transfer equation. *J Math Anal Appl* (2015) 429(1):415–38. doi:10.1016/j.jmaa.2015.03.079

52. Dong Y, Görner T, Kunis S. An algorithm for total variation regularized photoacoustic imaging. *Adv Comput Math* (2015) 41(2):423–38. doi:10.1007/s10444-014-9364-1

53. Biton S, Arbel N, Drozdov G, Gilboa G, Rosenthal A. Optoacoustic model-based inversion using anisotropic adaptive total-variation regularization. *Photoacoustics* (2019) 16:100142. doi:10.1016/j.pacs.2019.100142

54. Kong Q, Gong R, Liu J, Shao X. Investigation on reconstruction for frequency domain photoacoustic imaging via TVAL3 regularization algorithm. *IEEE Photon J* (2018) 10(5):1–15. doi:10.1109/jphot.2018.2869815

55. Ding L, Razansky D, Deán-Ben XL. Model-based reconstruction of large three-dimensional optoacoustic datasets. *IEEE Trans Med Imaging* (2020) 39(9):2931–40. doi:10.1109/tmi.2020.2981835

56. Bredies K, Nuster R, Watschinger R. TGV-regularized inversion of the Radon transform for photoacoustic tomography. *Biomed Opt Express* (2020) 11(2):994–1019. doi:10.1364/boe.379941

57. Ding L, Deán-Ben XL, Lutzweiler C, Razansky D, Ntziachristos V. *Phys Med Biol* (2015) 60(17):6733.

58. Poudel J, Lou Y, Anastasio MA. A survey of computational frameworks for solving the acoustic inverse problem in three-dimensional photoacoustic computed tomography. *Phys Med Biol* (2019) 64(14):14TR01. doi:10.1088/1361-6560/ab2017

59. Deán-Ben XL, Ding L, Razansky D. Dynamic particle enhancement in limited-view optoacoustic tomography. *Opt Lett* (2017) 42(4):827–30. doi:10.1364/ol.42.000827

60. Han Y, Ding L, Ben XLD, Razansky D, Prakash J, Ntziachristos V. Three-dimensional optoacoustic reconstruction using fast sparse representation. *Opt Lett* (2017) 42(5):979–82. doi:10.1364/ol.42.000979

61. Frikel J, Haltmeier M. Efficient regularization with wavelet sparsity constraints in photoacoustic tomography. *Inverse Probl* (2018) 34(2):024006. doi:10.1088/1361-6420/aaa0ac

62. Schoeder S, Olefir I, Kronbichler M, Ntziachristos V, Wall W. Optoacoustic image reconstruction: The full inverse problem with variable bases. *Proc R Soc A* (2018) 474(2219):20180369. doi:10.1098/rspa.2018.0369

63. Singh MKA, Sato N, Ichihashi F, Sankai Y. *Springer* (2020) 10:978–81.

64. Mohajerani P, Kellnberger S, Ntziachristos V. Frequency domain optoacoustic tomography using amplitude and phase. *Photoacoustics* (2014) 2(3):111–8. doi:10.1016/j.pacs.2014.06.002

65. Hirsch L, Gonzalez M, Rey Vega L. On the robustness of model-based algorithms for photoacoustic tomography: Comparison between time and frequency domains. *Rev Scientific Instr* (2021) 92(11):114901. doi:10.1063/5.0065966

66. Zhou Y, Yao J, Wang LV. Tutorial on photoacoustic tomography. *J Biomed Opt* (2016) 21(6):061007. doi:10.1117/1.jbo.21.6.061007

67. Cox BT, Kara S, Arridge SR, Beard PC. k-space propagation models for acoustically heterogeneous media: Application to biomedical photoacoustics. *J Acoust Soc Am* (2007) 121(6):3453–64. doi:10.1121/1.2717409

68. Rosenthal A, Razansky D, Ntziachristos V. Fast semi-analytical model-based acoustic inversion for quantitative optoacoustic tomography. *IEEE Trans Med Imaging* (2010) 29(6):1275–85. doi:10.1109/tmi.2010.2044584

69. Ding L, Deán-Ben XL, Razansky D. Real-time model-based inversion in cross-sectional optoacoustic tomography. *IEEE Trans Med Imaging* (2016) 35(8):1883–91. doi:10.1109/tmi.2016.2536779

70. Scruby CB, Drain LE. *Laser ultrasonics: Techniques and applications*. New York: Taylor & Francis Group (2019).

71. Deán-Ben XL, Özbek A, López-Schier H, Razansky D. Acoustic scattering mediated single detector optoacoustic tomography. *Phys Rev Lett* (2019) 123(17):174301. doi:10.1103/physrevlett.123.174301

72. Rosenthal A, Ntziachristos V, Razansky D. Model-based optoacoustic inversion with arbitrary-shape detectors. *Med Phys* (2011) 38(7):4285–95. doi:10.1118/1.3589141

73. Queirós D, Déan-Ben XL, Buehler A, Razansky D, Rosenthal A, Ntziachristos V. Modeling the shape of cylindrically focused transducers in three-dimensional optoacoustic tomography. *J Biomed Opt* (2013) 18(7):076014. doi:10.1117/1.jbo.18.7.076014

74. Ding L, Dean-Ben XL, Razansky D. Efficient 3-D model-based reconstruction scheme for arbitrary optoacoustic acquisition geometries. *IEEE Trans Med Imaging* (2017) 36(9):1858–67. doi:10.1109/tmi.2017.2704019

75. Lutzweiler C, Deán-Ben XL, Razansky D. Expediting model-based optoacoustic reconstructions with tomographic symmetries. *Med Phys* (2014) 41(1):013302. doi:10.1118/1.4846055

76. Li W, Hofmann UA, Rebling J, Zhou Q, Chen Z, Ozbek A, et al. Broadband model-based optoacoustic mesoscopy enables deep-tissue imaging beyond the acoustic diffraction limit. *Laser Photon Rev* (2022) 16(5):2100381. doi:10.1002/lpor.202100381

77. Aguirre J, Giannoula A, Minagawa T, Funk L, Turon P, Durduran T. A low memory cost model based reconstruction algorithm exploiting translational symmetry for photoacustic microscopy. *Biomed Opt Express* (2013) 4(12):2813–27. doi:10.1364/boe.4.002813

78. Arridge SR, Betcke MM, Cox BT, Lucka F, Treeby BE. On the adjoint operator in photoacoustic tomography. *Inverse Probl* (2016) 32(11):115012. doi:10.1088/0266-5611/32/11/115012

79. Turin G. An introduction to matched filters. *IEEE Trans Inf Theor* (1960) 6(3):311–29. doi:10.1109/tit.1960.1057571

80. Willemink MJ, Noël PB. The evolution of image reconstruction for CT—From filtered back projection to artificial intelligence. *Eur Radiol* (2019) 29(5):2185–95. doi:10.1007/s00330-018-5810-7

81. Andreev VG, Popov DV, Sushko DV, Karabutov AA, Oraevsky AA. *Inverse Radon transform for optoacoustic imaging*. SPIE: Biomedical Optoacoustics II (2001). p. 119–29.

82. Xu M, Xu Y, Wang LV. Time-domain reconstruction algorithms and numerical simulations for thermoacoustic tomography in various geometries. *IEEE Trans Biomed Eng* (2003) 50(9):1086–99. doi:10.1109/TBME.2003.816081

83. Özbek A, Deán-Ben XL, Razansky D. *IEEE Trans Med Imaging* (2022).

84. Taruttis A, Ntziachristos V. Advances in real-time multispectral optoacoustic imaging and its applications. *Nat Photon* (2015) 9(4):219–27. doi:10.1038/nphoton.2015.29

85. Deán-Ben XL, Merčep E, Razansky D. Hybrid-array-based optoacoustic and ultrasound (OPUS) imaging of biological tissues. *Appl Phys Lett* (2017) 110(20):203703. doi:10.1063/1.4983462

86. Jetzfellner T, Rosenthal A, Englmeier K-H, Dima A, Caballero MÁA, Razansky D, et al. Interpolated model-matrix optoacoustic tomography of the mouse brain. *Appl Phys Lett* (2011) 98(16):163701. doi:10.1063/1.3579156

87. Regensburger AP, Fonteyne LM, Jüngert J, Wagner AL, Gerhalter T, Nagel AM, et al. Detection of collagens by multispectral optoacoustic tomography as an imaging biomarker for Duchenne muscular dystrophy. *Nat Med* (2019) 25(12):1905–15. doi:10.1038/s41591-019-0669-y

88. Ivankovic I, Merčep E, Schmedt C-G, Deán-Ben XL, Razansky D. Real-time volumetric assessment of the human carotid artery: Handheld multispectral optoacoustic tomography. *Radiology* (2019) 291(1):45–50. doi:10.1148/radiol.2019181325

89. Hu P, Li L, Lin L, Wang LV. Spatiotemporal antialiasing in photoacoustic computed tomography. *IEEE Trans Med Imaging* (2020) 39(11):3535–47. doi:10.1109/tmi.2020.2998509

90. Shen K, Liu S, Feng T, Yuan J, Zhu B, Tian C. Negativity artifacts in back-projection based photoacoustic tomography. *J Phys D Appl Phys* (2020) 54(7):074001. doi:10.1088/1361-6463/abc37d

91. Ding L, Deán-Ben XL, Lutzweiler C, Razansky D, Ntziachristos V. Image reconstruction in cross-sectional optoacoustic tomography based on non-negative constrained model-based inversion. In: European Conference on Biomedical Optics. Washington, DC: Optica Publishing Group (2015). p. 953919.

92. Burgholzer P, Bauer-Marschallinger J, Haltmeier M. Breaking the resolution limit in photoacoustic imaging using non-negativity and sparsity. *Photoacoustics* (2020) 19:100191. doi:10.1016/j.pacs.2020.100191

93. Egolf D, Barber Q, Zemp R. Single laser-shot super-resolution photoacoustic tomography with fast sparsity-based reconstruction. *Photoacoustics* (2021) 22:100258. doi:10.1016/j.pacs.2021.100258

94. Wang J, Zhang C, Wang Y. *Biomed Eng Online* (2017) 16(1):1–30.

95. Yao L, Jiang H. Enhancing finite element-based photoacoustic tomography using total variation minimization. *Appl Opt* (2011) 50(25):5031–41. doi:10.1364/ao.50.005031

96. Zhang Y, Wang Y, Zhang C. Total variation based gradient descent algorithm for sparse-view photoacoustic image reconstruction. *Ultrasonics* (2012) 52(8): 1046–55. doi:10.1016/j.ultras.2012.08.012

97. Tarvainen T, Cox BT, Kaipio J, Arridge SR. Reconstructing absorption and scattering distributions in quantitative photoacoustic tomography. *Inverse Probl* (2012) 28(8):084009. doi:10.1088/0266-5611/28/8/084009

98. Yalavarthy PK, Kalva SK, Pramanik M, Prakash J. Non-local means improves total-variation constrained photoacoustic image reconstruction. *J Biophotonics* (2021) 14(1):e202000191. doi:10.1002/jbio.202000191

99. Özbek A, Deán-Ben XL, Razansky D. Optoacoustic imaging at kilohertz volumetric frame rates. *Optica* (2018) 5(7):857–63. doi:10.1364/optica.5.000857

100. Özsoy Ç, Özbek A, Reiss M, Deán-Ben XL, Razansky D. Ultrafast four-dimensional imaging of cardiac mechanical wave propagation with sparse optoacoustic sensing. *Proc Natl Acad Sci U S A* (2021) 118(45):e2103979118. doi:10.1073/pnas.2103979118

101. Hauptmann A, Lucka F, Betcke M, Huynh N, Adler J, Cox B, et al. Model-based learning for accelerated, limited-view 3-D photoacoustic tomography. *IEEE Trans Med Imaging* (2018) 37(6):1382–93. doi:10.1109/tmi.2018.2820382

102. Caballero MAA, Rosenthal A, Buehler A, Razansky D, Ntziachristos V. Optoacoustic determination of spatio- temporal responses of ultrasound sensors. *IEEE Trans Ultrason Ferroelectr Freq Control* (2013) 60(6):1234–44. doi:10.1109/tuffc.2013.2687

103. Li M-L, Tseng Y-C, Cheng C-C. Model-based correction of finite aperture effect in photoacoustic tomography. *Opt Express* (2010) 18(25):26285–92. doi:10.1364/oe.18.026285

104. Hoelen CG, de Mul FF. Image reconstruction for photoacoustic scanning of tissue structures. *Appl Opt* (2000) 39(31):5872–83. doi:10.1364/ao.39.005872

105. Luo X, Xiao J, Wang C, Wang B. Fast correction of "finite aperture effect" in photoacoustic tomography based on spatial impulse response. *Photonics* (2021) 8(9):356. doi:10.3390/photonics8090356

106. Mitsuhashi K, Wang K, Anastasio MA. Investigation of the far-field approximation for modeling a transducer's spatial impulse response in photoacoustic computed tomography. *Photoacoustics* (2014) 2(1):21–32. doi:10.1016/j.pacs.2013.11.001

107. Steinberg I, Kim J, Schneider MK, Hyun D, Zlitni A, Hopper SM, et al. Superiorized photo-acoustic non-NEgative reconstruction (SPANNER) for clinical photoacoustic imaging. *IEEE Trans Med Imaging* (2021) 40(7):1888–97. doi:10.1109/tmi.2021.3068181

108. Shang R, Archibald R, Gelb A, Luke GP. Sparsity-based photoacoustic image reconstruction with a linear array transducer and direct measurement of the forward model. *J Biomed Opt* (2018) 24(3):1. doi:10.1117/1.jbo.24.3.031015

109. Prakash R, Badal D, Paul A, Sonker D, Saha RK. Photoacoustic signal simulation using discrete particle approach and its application in tomography. *IEEE Trans Ultrason Ferroelectr Freq Control* (2020) 68(3):707–17. doi:10.1109/tuffc.2020.3022937

110. Vilov S, Arnal B, Hojman E, Eldar YC, Katz O, Bossy ES. *reports* (2020) 10(1):1–8.

111. Seeger M, Soliman D, Aguirre J, Diot G, Wierzbowski J, Ntziachristos V. Pushing the boundaries of optoacoustic microscopy by total impulse response characterization. *Nat Commun* (2020) 11(1):2910–3. doi:10.1038/s41467-020-16565-2

112. Lu Q-B, Liu T, Ding L, Lu M-H, Zhu J, Chen Y-F. Probing the spatial impulse response of ultrahigh-frequency ultrasonic transducers with photoacoustic waves. *Phys Rev Appl* (2020) 14(3):034026. doi:10.1103/physrevapplied.14.034026

113. Al. UHe. *Under review*.

114. Luís Dean-Ben X, Razansky D. Localization optoacoustic tomography. *Light Sci Appl* (2018) 7(4):18004. doi:10.1038/lsa.2018.4

115. Nozdriukhin D, Kalva SK, Li W, Yashchenok A, Gorin D, Razansky D, et al. Rapid volumetric optoacoustic tracking of individual microparticles *in vivo* enabled by a NIR-absorbing gold–carbon shell. *ACS Appl Mater Inter* (2021) 13(41): 48423–32. doi:10.1021/acsami.1c15509

116. Degtyaruk O, Nozdriukhin D, Razansky D, Deán-Ben XL. *In situ* characterization of microparticulate optoacoustic contrast agents in an intracardiac perfusion mouse model. *Opt Lett* (2021) 46(17):4350–3. doi:10.1364/ol.435360

117. Szabo TL. *Diagnostic ultrasound imaging: Inside out*. Academic Press (2004).

118. Deán-Ben XL, Ntziachristos V, Razansky D. Effects of small variations of speed of sound in optoacoustic tomographic imaging. *Med Phys* (2014) 41(7): 073301. doi:10.1118/1.4875691

119. Singh MKA, Steenbergen W. *Photoacoustics* (2015) 3(4):123–31.

120. Allman D, Reiter A, Bell MAL. Photoacoustic source detection and reflection artifact removal enabled by deep learning. *IEEE Trans Med Imaging* (2018) 37(6): 1464–77. doi:10.1109/tmi.2018.2829662

121. Deán-Ben XL, Ntziachristos V, Razansky D. Artefact reduction in optoacoustic tomographic imaging by estimating the distribution of acoustic scatterers. *J Biomed Opt* (2012) 17(11):110504. doi:10.1117/1.jbo.17.11.110504

122. Treeby BE. Acoustic attenuation compensation in photoacoustic tomography using time-variant filtering. *J Biomed Opt* (2013) 18(3):036008. doi:10.1117/1.jbo.18.3.036008

123. Deán-Ben XL, Razansky D, Ntziachristos V. *Phys Med Biol* (2011) 56(18): 6129.

124. Huang C, Wang K, Nie L, Wang LV, Anastasio MA. Full-wave iterative image reconstruction in photoacoustic tomography with acoustically inhomogeneous media. *IEEE Trans Med Imaging* (2013) 32(6):1097–110. doi:10.1109/tmi.2013.2254496

125. Haltmeier M, Nguyen LV. Analysis of iterative methods in photoacoustic tomography with variable sound speed. *SIAM J Imaging Sci* (2017) 10(2):751–81. doi:10.1137/16m1104822

126. Yuan Z, Jiang H. Three-dimensional finite-element-based photoacoustic tomography: Reconstruction algorithm and simulations. *Med Phys* (2007) 34(2): 538–46. doi:10.1118/1.2409234

127. Ding T, Ren K, Vallélian S. A one-step reconstruction algorithm for quantitative photoacoustic imaging. *Inverse Probl* (2015) 31(9):095005. doi:10.1088/0266-5611/31/9/095005

128. Cai C, Wang X, Deng K, Luo J, Ma C. Photoacoustic computed tomography for joint reconstruction of initial pressure and sound speed in vivo using a feature coupling method. In: European Conference on Biomedical Optics. Washington, DC: Optica Publishing Group (2019). p. 11077_12.

129. Matthews TP, Poudel J, Li L, Wang LV, Anastasio MA. Parameterized joint reconstruction of the initial pressure and sound speed distributions for photoacoustic computed tomography. *SIAM J Imaging Sci* (2018) 11(2): 1560–88. doi:10.1137/17m1153649

130. Perez-Liva M, Udías JM, Camacho J, Merčep E, Deán-Ben XL, Razansky D, et al. Speed of sound ultrasound transmission tomography image reconstruction based on Bézier curves. *Ultrasonics* (2020) 103:106097. doi:10.1016/j.ultras.2020.106097

131. Yang H, Prakash J, Ntziachristos V.

132. Deán-Ben XL, Pang GA, Montero de Espinosa F, Razansky D. Non-contact optoacoustic imaging with focused air-coupled transducers. *Appl Phys Lett* (2015) 107(5):051105. doi:10.1063/1.4928123

133. Özsoy C, Xu J, Li J, Montero de Espinosa F, Razansky D, Deán-Ben XL. Optoacoustic imaging with an air-coupled transducer using coaxially aligned focused illumination. *AIP Adv* (2022) 12(3):035043. doi:10.1063/5.0078053

134. Merčep E, Herraiz JL, Deán-Ben XL, Razansky DL. *Sci Appl* (2019) 8(1):1–12.

135. Deán-Ben XL, Ma R, Rosenthal A, Ntziachristos V, Razansky D. *Phys Med Biol* (2013) 58(16):5555.

136. Dean-Ben XL, Ma R, Razansky D, Ntziachristos V. Statistical approach for optoacoustic image reconstruction in the presence of strong acoustic heterogeneities. *IEEE Trans Med Imaging* (2010) 30(2):401–8. doi:10.1109/tmi.2010.2081683

137. Deán-Ben XL, Ntziachristos V, Razansky D. Statistical optoacoustic image reconstruction using a-priori knowledge on the location of acoustic distortions. *Appl Phys Lett* (2011) 98(17):171110. doi:10.1063/1.3564905

138. Muhammad M, Prakash J, Liapis E, Ntziachristos V, Jüstel D. Weighted model-based optoacoustic reconstruction for partial-view geometries. *J Biophotonics* (2022) 15:e202100334. doi:10.1002/jbio.202100334

139. Estrada H, Rebling J, Turner J, Razansky D. Broadband acoustic properties of a murine skull. *Phys Med Biol* (2016) 61(5):1932–46. doi:10.1088/0031-9155/61/5/1932

140. Estrada H, Gottschalk S, Reiss M, Neuschmelting V, Goldbrunner R, Razansky D. Observation of guided acoustic waves in a human skull. *Ultrasound Med Biol* (2018) 44(11):2388–92. doi:10.1016/j.ultrasmedbio.2018.05.019

141. Poudel J, Na S, Wang LV, Anastasio MA. Iterative image reconstruction in transcranial photoacoustic tomography based on the elastic wave equation. *Phys Med Biol* (2020) 65(5):055009. doi:10.1088/1361-6560/ab6b46

142. Dean-Ben XL, Razansky D. *arXiv preprint* (2021). arXiv:2108.03958.

143. Eldar YC, Kutyniok G. *Compressed sensing: Theory and applications*. Cambridge University Press (2012).

144. Provost J, Lesage F. The application of compressed sensing for photo-acoustic tomography. *IEEE Trans Med Imaging* (2008) 28(4):585–94. doi:10.1109/tmi.2008.2007825

145. Guo Z, Li C, Song L, Wang LV. Compressed sensing in photoacoustic tomography *in vivo*. *J Biomed Opt* (2010) 15(2):021311. doi:10.1117/1.3381187

146. Haltmeier M, Berer T, Moon S, Burgholzer P. Compressed sensing and sparsity in photoacoustic tomography. *J Opt* (2016) 18(11):114004. doi:10.1088/2040-8978/18/11/114004

147. Ntziachristos V, Rosenthal A. Compressed system models in multispectral optoacoustic tomography. In *IEEE 12th international symposium on biomedical imaging*. IEEE (2015). p. 1228–31.

148. Meng J, Wang LV, Ying L, Liang D, Song L. Compressed-sensing photoacoustic computed tomography *in vivo* with partially known support. *Opt Express* (2012) 20(15):16510–23. doi:10.1364/oe.20.016510

149. Gao M, Si G, Bai Y, Wang LV, Liu C, Meng J. Graphics processing unit accelerating compressed sensing photoacoustic computed tomography with total variation. *Appl Opt* (2020) 59(3):712–9. doi:10.1364/ao.378466

150. Li Y, Li L, Zhu L, Maslov K, Shi J, Hu P, et al. Snapshot photoacoustic topography through an ergodic relay for high-throughput imaging of optical absorption. *Nat Photon* (2020) 14(3):164–70. doi:10.1038/s41566-019-0576-2

151. Brown M, Zhang E, Treeby B, Beard P, Cox B. Reverberant cavity photoacoustic imaging. *Optica* (2019) 6(6):821–2. doi:10.1364/optica.6.000821

152. Wang LV. *Photoacoustic imaging and spectroscopy*. Boca Raton, FL: CRC Press (2017).

153. Gusev VĖ, Gusev V, Karabutov A. *Laser optoacoustics*. American Institute of Physics (1993).

154. Bates R, Robinson B. Ultrasonic transmission speckle imaging. *Ultrason Imaging* (1981) 3(4):378–94. doi:10.1177/016173468100300407

155. Li M, Tang Y, Yao J. Photoacoustic tomography of blood oxygenation: A mini review. *Photoacoustics* (2018) 10:65–73. doi:10.1016/j.pacs.2018.05.001

156. Cox BT, Laufer JG, Beard PC, Arridge SR. Quantitative spectroscopic photoacoustic imaging: A review. *J Biomed Opt* (2012) 17(6):061202. doi:10.1117/1.jbo.17.6.061202

157. Gujrati V, Mishra A, Ntziachristos V. Molecular imaging probes for multi-spectral optoacoustic tomography. *Chem Commun* (2017) 53(34):4653–72. doi:10.1039/c6cc09421j

158. Basak K, Deán-Ben L, Gottschalk S, Reiss M, Razansky DL. *Sci Appl* (2019) 8(1):1–10.

159. Robin J, Rau R, Lafci B, Schroeter A, Reiss M, Deán-Ben X-L, et al. Hemodynamic response to sensory stimulation in mice: Comparison between functional ultrasound and optoacoustic imaging. *NeuroImage* (2021) 237:118111. doi:10.1016/j.neuroimage.2021.118111

160. Ding L, Deán-Ben XL, Burton NC, Sobol RW, Ntziachristos V, Razansky D. Constrained inversion and spectral unmixing in multispectral optoacoustic tomography. *IEEE Trans Med Imaging* (2017) 36(8):1676–85. doi:10.1109/tmi.2017.2686006

161. Bu S, Liu Z, Shiina T, Kondo K, Yamakawa M, Fukutani K, et al. Model-based reconstruction integrated with fluence compensation for photoacoustic tomography. *IEEE Trans Biomed Eng* (2012) 59(5):1354–63. doi:10.1109/TBME.2012.2187649

162. Pattyn A, Mumm Z, Alijabbari N, Duric N, Anastasio MA, Mehrmohammadi M. Model-based optical and acoustical compensation for photoacoustic tomography of heterogeneous mediums. *Photoacoustics* (2021) 23:100275. doi:10.1016/j.pacs.2021.100275

163. Daoudi K, Hussain A, Hondebrink E, Steenbergen W. Correcting photoacoustic signals for fluence variations using acousto-optic modulation. *Opt Express* (2012) 20(13):14117–29. doi:10.1364/oe.20.014117

164. Deán-Ben XL, Stiel AC, Jiang Y, Ntziachristos V, Westmeyer GG, Razansky D. Light fluence normalization in turbid tissues via temporally unmixed multispectral optoacoustic tomography. *Opt Lett* (2015) 40(20):4691–4. doi:10.1364/ol.40.004691

165. Deán-Ben XL, Robin J, Ni R, Razansky D. *arXiv preprint arXiv* (2020). 2007.00372.

166. Gröhl J, Schellenberg M, Dreher K, Maier-Hein L. Deep learning for biomedical photoacoustic imaging: A review. *Photoacoustics* (2021) 22:100241. doi:10.1016/j.pacs.2021.100241

167. Yang C, Lan H, Gao F, Gao F. Review of deep learning for photoacoustic imaging. *Photoacoustics* (2021) 21:100215. doi:10.1016/j.pacs.2020.100215

168. Antholzer S, Haltmeier M, Schwab J. Deep learning for photoacoustic tomography from sparse data. *Inverse Probl Sci Eng* (2019) 27(7):987–1005. doi:10.1080/17415977.2018.1518444

169. Deng H, Qiao H, Dai Q, Ma C. Deep learning in photoacoustic imaging: A review. *J Biomed Opt* (2021) 26(4):040901. doi:10.1117/1.jbo.26.4.040901

170. Godefroy G, Arnal B, Bossy E. Compensating for visibility artefacts in photoacoustic imaging with a deep learning approach providing prediction uncertainties. *Photoacoustics* (2021) 21:100218. doi:10.1016/j.pacs.2020.100218

171. Davoudi N, Deán-Ben XL, Razansky D. Deep learning optoacoustic tomography with sparse data. *Nat Mach Intell* (2019) 1(10):453–60. doi:10.1038/s42256-019-0095-3

172. Lafci B, Merčep E, Morscher S, Deán-Ben XL, Razansky D. Deep learning for automatic segmentation of hybrid optoacoustic ultrasound (OPUS) images. *IEEE Trans Ultrason Ferroelectr Freq Control* (2020) 68(3):688–96. doi:10.1109/tuffc.2020.3022324

173. Olefir I, Tzoumas S, Restivo C, Mohajerani P, Xing L, Ntziachristos V. Deep learning-based spectral unmixing for optoacoustic imaging of tissue oxygen saturation. *IEEE Trans Med Imaging* (2020) 39(11):3643–54. doi:10.1109/tmi.2020.3001750

174. Hu Y, Lafci B, Luzgin A, Wang H, Klohs J, Dean-Ben XL, et al. *arXiv preprint* (2021). arXiv:2109.01880.

175. Hauptmann A, Cox BT. Deep learning in photoacoustic tomography: Current approaches and future directions. *J Biomed Opt* (2020) 25(11):112903. doi:10.1117/1.jbo.25.11.112903

176. Hsu K-T, Guan S, Chitnis PV. Comparing deep learning frameworks for photoacoustic tomography image reconstruction. *Photoacoustics* (2021) 23:100271. doi:10.1016/j.pacs.2021.100271

177. Davoudi N, Lafci B, Özbek A, Deán-Ben XL, Razansky D. Deep learning of image- and time-domain data enhances the visibility of structures in optoacoustic tomography. *Opt Lett* (2021) 46(13):3029–32. doi:10.1364/ol.424571

178. Lan H, Jiang D, Gao F, Gao F. Deep learning enabled real-time photoacoustic tomography system via single data acquisition channel. *Photoacoustics* (2021) 22:100270. doi:10.1016/j.pacs.2021.100270

179. Dehner C, Zahnd G, Ntziachristos V, Jüstelpreprint D *arXiv:2206.14485* (2022).

180. Antholzer S, Schwab J, Bauer-Marschallinger J, Burgholzer P, Haltmeier M, NETT regularization for compressed sensing photoacoustic tomography. In *Photons plus ultrasound: Imaging and sensing*. 2019. Bellingham: SPIE (2019). p. 272–82.

181. Gong J, Lan H, Gao F, Gao F. *Deep learning regularized acceleration for photoacoustic image reconstruction*. In: *2021 IEEE international ultrasonics symposium (IUS)*. IEEE (2021). p. 1–4.